Quantum Photonics

Edited by

Yasuhiko Arakawa
Institute for Nano Quantum Information Electronics, The University of Tokyo, Tokyo, Japan

Dieter Bimberg
Center of Nanophotonics, Technical University of Berlin, Berlin, Germany and Bimberg Chinese-German Center for Green Photonics, CIOMP, Chinese Academy of Sciences, Changchun, China

ELSEVIER

Elsevier
Radarweg 29, PO Box 211, 1000 AE Amsterdam, Netherlands
125 London Wall, London EC2Y 5AS, United Kingdom
50 Hampshire Street, 5th Floor, Cambridge, MA 02139, United States

Publisher's note: Elsevier takes a neutral position with respect to territorial disputes or jurisdictional claims in its published content, including in maps and institutional affiliations.

Notices
Knowledge and best practice in this field are constantly changing. As new research and experience broaden our understanding, changes in research methods, professional practices, or medical treatment may become necessary.

Practitioners and researchers must always rely on their own experience and knowledge in evaluating and using any information, methods, compounds, or experiments described herein. In using such information or methods they should be mindful of their own safety and the safety of others, including parties for whom they have a professional responsibility.

To the fullest extent of the law, neither the Publisher nor the authors, contributors, or editors, assume any liability for any injury and/or damage to persons or property as a matter of products liability, negligence or otherwise, or from any use or operation of any methods, products, instructions, or ideas contained in the material herein.

ISBN: 978-0-323-98378-5

Publisher: Matthew Deans
Acquisitions Editor: Stephen Jones
Editorial Project Manager: Palak Gupta
Production Project Manager: Anitha Sivaraj
Cover Designer: Greg Harris

Typeset by STRAIVE, India

Contents

Contributors

Takao Aoki Department of Applied Physics, Waseda University, Shinjuku-ku, Tokyo, Japan

Yasuhiko Arakawa Institute for Nano Quantum Information Electronics, The University of Tokyo, Tokyo, Japan

Takashi Asano Department of Electronic Science and Engineering, Kyoto University, Kyoto-Daigaku-Katsura, Nishikyo-ku, Kyoto, Japan

Simon Betzold Julius-Maximilians-Universität Würzburg, Physikalisches Institut and Würzburg-Dresden Cluster of Excellence ct.qmat, Lehrstuhl für Technische Physik, Am Hubland, Würzburg, Germany

Dieter Bimberg Center of Nanophotonics, Technical University of Berlin, Berlin, Germany; Bimberg Chinese-German Center for Green Photonics, CIOMP, Chinese Academy of Sciences, Changchun, China

Julien Claudon Equipe Nanophysique et Semiconducteurs, Université Grenoble-Alpes, CEA, INP, IRIG-PHELIQS, Grenoble, France

Bozhang Dong Institute for Energy Efficiency, University of California Santa Barbara, Santa Barbara, CA, United States

Jianan Duan School of Electronic and Information Engineering, Harbin Institute of Technology, Shenzhen, China

Kosuke Fukui Department of Applied Physics, The University of Tokyo, Tokyo, Japan

Jean-Michel Gérard Equipe Nanophysique et Semiconducteurs, Université Grenoble-Alpes, CEA, INP, IRIG-PHELIQS, Grenoble, France

Frédéric Grillot Télécom Paris, Institut Polytechnique de Paris, Palaiseau, France; Center for High Technology Material, University of New Mexico, Albuquerque, NM, United States

Sven Höfling Julius-Maximilians-Universität Würzburg, Physikalisches Institut and Würzburg-Dresden Cluster of Excellence ct.qmat, Lehrstuhl für Technische Physik, Am Hubland, Würzburg, Germany

Heming Huang Télécom Paris, Institut Polytechnique de Paris, Palaiseau, France

Hidetoshi Katori Quantum Metrology Laboratory; Space-Time Engineering Research Team, RIKEN, Wako, Saitama; Department of Applied Physics, Graduate School of Engineering, The University of Tokyo, Bunkyo-Ku, Tokyo, Japan

Sebastian Klembt Julius-Maximilians-Universität Würzburg, Physikalisches Institut and Würzburg-Dresden Cluster of Excellence ct.qmat, Lehrstuhl für Technische Physik, Am Hubland, Würzburg, Germany

Ryotaro Konoike Photonics Research Center, National Institute of Advanced Industrial Science and Technology (AIST), Tsukuba, Japan

Peter Michler Institute of Semiconductor Optics and Functional Interfaces, University of Stuttgart, Stuttgart, Germany

Norikazu Mizuochi Institute for Chemical Research; Center for Spintronics Research Network, Institute for Chemical Research, Kyoto University, Uji, Japan

Naoya Morioka Institute for Chemical Research; Center for Spintronics Research Network, Institute for Chemical Research, Kyoto University, Uji, Japan

Susumu Noda Department of Electronic Science and Engineering; Photonics and Electronics Science and Engineering Center, Kyoto University, Kyoto-Daigaku-Katsura, Nishikyo-ku, Kyoto, Japan

Simone Luca Portalupi Institute of Semiconductor Optics and Functional Interfaces, University of Stuttgart, Stuttgart, Germany

Stephan Reitzenstein Institute of Solid State Physics, Technical University of Berlin, Berlin, Germany

Sven Rodt Institute of Solid State Physics, Technical University of Berlin, Berlin, Germany

Andrei Schliwa Institute of Solid State Physics, Technical University Berlin, Berlin, Germany

Masao Takamoto Quantum Metrology Laboratory; Space-Time Engineering Research Team, RIKEN, Wako, Saitama, Japan

Shuntaro Takeda Department of Applied Physics, The University of Tokyo, Tokyo, Japan

Masahiro Takeoka Keio University, Yokohama, Kanagawa, Japan

Hüseyin Vural Institute of Semiconductor Optics and Functional Interfaces, University of Stuttgart, Stuttgart, Germany

Makoto Yamaguchi Department of Physics, Tokai University, Hiratsuka, Kanagawa, Japan

Introduction

1

Yasuhiko Arakawa[a] *and Dieter Bimberg*[b,c]
[a]Institute for Nano Quantum Information Electronics, The University of Tokyo, Tokyo, Japan, [b]Center of Nanophotonics, Technical University of Berlin, Berlin, Germany, [c]Bimberg Chinese-German Center for Green Photonics, CIOMP, Chinese Academy of Sciences, Changchun, China

1.1 Overview of quantum photonics

In this chapter, we will present a compressed flow of the progress of the various branches of quantum photonics. For more details, please refer to other chapters of this book or textbooks on quantum mechanics and classical photonics.

Quantum photonics is based on the merger of the classical experimental field of light with the theory of quantum mechanics. It has evolved into a field that is revolutionizing information processing, communication, and measurement technologies, where devices and systems have been researched and developed to control, manipulate, and exploit the quantum states of individual electron particles for a variety of applications, based on cutting-edge processing and material fabrication technologies.

The development of quantum mechanics in the first half of the 20th century (i.e., the dawn of quantum photonics) is reviewed here first. Quantum photonics has further developed during the second half of the 20th century, previously called "quantum electronics" or "optoelectronics," now often referred to as quantum 1.0. Semiconductor lasers are emphasized here as an example of quantum 1.0. Cavity electromagnetics are discussed next, and single photon sources will be mentioned as an example of nonclassical light sources, then concluding with a glimpse of quantum integrated photonics.

The number of quantum photonics applications is developing rapidly, innovating a variety of technological fields including computing, communications, sensing, and imaging. Typical areas based on quantum photonics will be discussed.

Quantum computers are systems that utilize the principles of quantum mechanics to perform calculations beyond the reach of classical computers. While superconducting circuit elements are typically used to construct qubits and quantum gated circuits, these systems use microwaves. Quantum interactions with laser light are used in trapped-ion qubits. Here, along with the increase in the number of qubits (nearly 1 million qubits are currently considered to be needed for practical use of fault-tolerant universal quantum computers), future challenges are maintaining coherence and minimizing errors.

Quantum communication based on quantum principles forms the basis of secure communication systems. Quantum Key Distribution (QKD) protocols using single photon sources enable secure transmission of cryptographic keys. The use of quantum

Quantum Photonics. https://doi.org/10.1016/B978-0-323-98378-5.00003-9

Quantum electrodynamics in optical microcavities and waveguides: Basics and applications to quantum photonics

2

Julien Claudon and Jean-Michel Gérard
Equipe Nanophysique et Semiconducteurs, Université Grenoble-Alpes, CEA, INP, IRIG-PHELIQS, Grenoble, France

2.1 Introduction

Photoluminescence properties, that is, how a material reemits light of a different color upon excitation by a light beam, are commonly seen as a characteristic property of that material. Photoluminescence spectroscopy is still widely used nowadays to characterize very diverse materials including semiconductors and precious gems. In his seminal paper on the quantum theory of radiation, Einstein assumed that an isolated excited atom would inevitably radiate, with a time constant defined by the two quantized electron states involved in the transition [1]. These views of spontaneous emission (SE) overlook the fact that SE results from the coupling of the excited emitter to a bath of modes of the electromagnetic field. In an attempt to control spin relaxation processes, Purcell was the first to realize in 1946 that SE dynamics can be modified by tailoring the modes to which the emitter is coupled [2]; more precisely, he predicted that SE would be accelerated for an emitter coupled to a single mode of an electromagnetic resonator.

In the 1980s, progress in experimental techniques in atomic physics and optics enabled exploring SE modifications for atoms in confined electromagnetic systems and building ground for the new field of cavity quantum electrodynamics (CQED) [3, 4]. The combination of flying Rydberg atoms and of (basically lossless) microwave cavities bounded by superconducting mirrors has been particularly fruitful, providing firm observations of enhanced and inhibited SE, as well as reversible SE in the so-called "strong coupling regime." Beyond their fundamental interest, these new effects opened the way to the development of new devices such as single-atom masers [4].

In the field of semiconductor sources of light, the 1980s have been marked by the mass-market use of quantum well (QW) laser diodes. Besides research aiming at optimizing their figures of merit, radically new concepts have been proposed to circumvent some intrinsic limitations of QW lasers, through a better control over SE: the

Quantum Photonics. https://doi.org/10.1016/B978-0-323-98378-5.00007-6

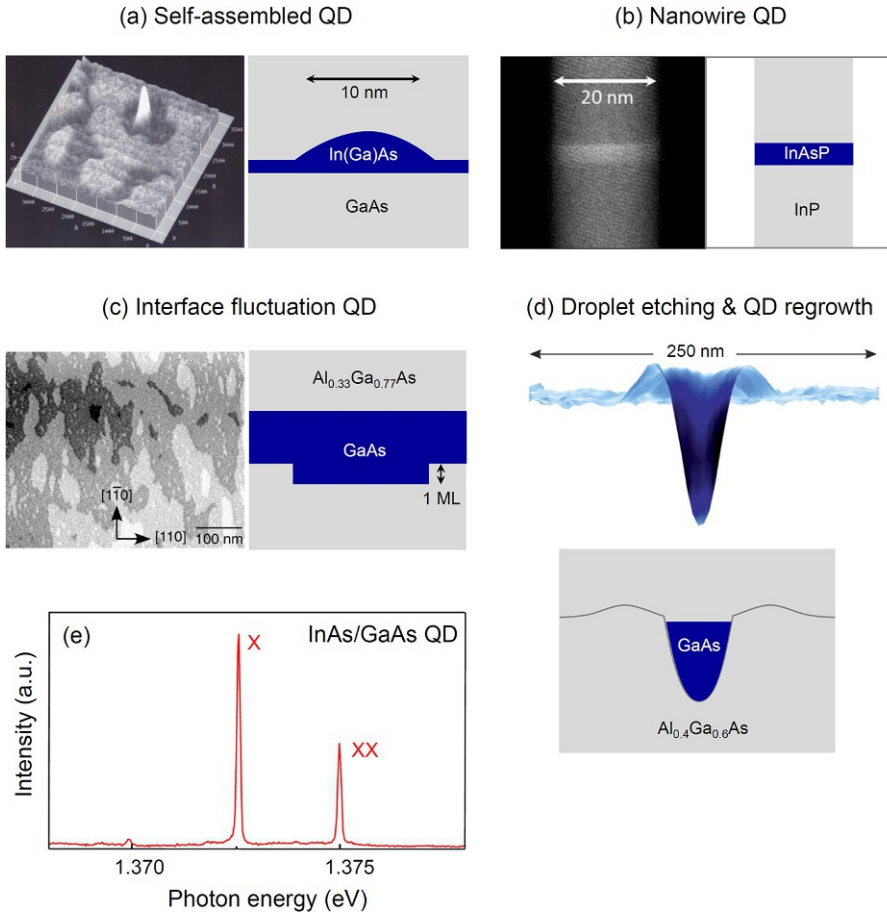

Fig. 2.1 Different flavors of artificial atoms. Examples of QDs fabricated using III–V semiconductor materials. (A) Self-assembled InAs/GaAs QD obtained by the Stranski-Krastanov method. The *left panel* is an AFM image of a single InAs QD (*light gray* structure), before capping by a top GaAs layer [25]. These QDs feature a flat lens morphology. (B) A nanowire QD is a longitudinal heterostructure, obtained during the axial growth of a nanowire (*left panel*: transmission electron microscopy image from Ref. [26]). To optimize the QD properties and the light extraction, the wire is very often capped by a shell, obtained by a subsequent radial growth (not shown). (C) An interface fluctuation QD is formed by thickness fluctuations of a quantum well (here GaAs in AlGaAs barriers). The *top panel* is an AFM image, showing the thickness fluctuations of the "bottom" AlGaAs surface, before the growth of the GaAs quantum well and of the top AlGaAs capping layer [27]. These QDs feature a lateral extension that is much larger than the one of self-assembled QDs, leading to a giant oscillator strength. (D) GaAs QD obtained by infilling nanoholes created by in situ droplet etching of AlGaAs layers. The *top panel* is a 3D rendering of an AFM image of the nanohole (the height-to-width ratio is amplified 17 times) [28]. (E) Microphotoluminescence spectrum of a single, self-assembled InAs/GaAs QD that is cooled down to cryogenic temperature ($T = 4$ K). The exciton line (X) corresponds to the recombination of a single-trapped electron-hole pair. The biexciton line (XX) corresponds to the recombination of an electron-hole pair, in the presence of another one.

The vectorial function $\mathbf{f}_{\mathbf{k}s}(\mathbf{r})$ describes the mode spatial profile:

$$\mathbf{f}_{\mathbf{k}s}(\mathbf{r}) = \mathbf{e}_{\mathbf{k}s} e^{i\mathbf{k}\cdot\mathbf{r}}. \tag{2.3}$$

For a given $\mathbf{k}$, there are two possible transverse polarizations $\mathbf{e}_{\mathbf{k}s}$ ($s = 1, 2$). The polarization vectors can be complex (e.g., to describe a circular polarization). They are normalized and mutually orthogonal: $\mathbf{e}_{\mathbf{k}s}{}^{*}\cdot\mathbf{e}_{\mathbf{k}s'} = \delta_{ss'}$. Since the emitter is linearly polarized, we also choose a linear polarization basis for the modes; $\mathbf{e}_{\mathbf{k}1}$ and $\mathbf{e}_{\mathbf{k}2}$ are then real unit vectors. The mode spatial profile $\mathbf{f}_{\mathbf{k}s}(\mathbf{r})$ is obtained by solving the *classical* Maxwell equations, and by imposing the normalization condition: $\max_{\mathbf{r}}|\mathbf{f}_{\mathbf{k}s}(\mathbf{r})| = 1$. In Eq. (2.2), $\hat{a}_{\mathbf{k}s}$ and $\hat{a}^{\dagger}_{\mathbf{k}s}$ are the photon annihilation and photon creation operators of mode $\{\mathbf{k}, s\}$, respectively; $\hat{a}_{\mathbf{k}s}$ and $\hat{a}^{\dagger}_{\mathbf{k}s}$ satisfy the usual commutation relations in multimode bosonic systems. Finally, the normalization factor reads

$$\mathcal{E}_{\omega_{\mathbf{k}}} = \sqrt{\frac{\hbar\omega_{\mathbf{k}}}{2\epsilon_0 n^2 L^3}}. \tag{2.4}$$

It corresponds to the r.m.s. value of the zero-point fluctuations of the electrical field of mode $\{\mathbf{k}, s\}$ ($\langle 0_{\mathbf{k}s}|\hat{\mathbf{E}}^2_{\mathbf{k}s}(\mathbf{r})|0_{\mathbf{k}s}\rangle = \mathcal{E}^2_{\omega_{\mathbf{k}}}$).

2.3.2.2 Light-matter Hamiltonian

The emitter-radiation field dynamics is governed by the Hamiltonian:

$$\hat{H} = \underbrace{\frac{1}{2}\hbar\omega_{\mathrm{eg}}\hat{\sigma}_z}_{\text{Emitter}} + \underbrace{\sum_{\mathbf{k},s}\hbar\omega_{\mathbf{k}}\left(\hat{a}^{\dagger}_{\mathbf{k}s}\hat{a}_{\mathbf{k}s} + \frac{1}{2}\right)}_{\text{Radiation field}} \underbrace{-\hat{\mathbf{d}}\cdot\hat{\mathbf{E}}(\mathbf{0})}_{\text{Dipole interaction}}. \tag{2.5}$$

The first term is associated with the isolated two-level emitter; $\hat{\sigma}_z$ is the Pauli operator $\hat{\sigma}_z = |e\rangle\langle e| - |g\rangle\langle g|$. The radiation field is described as a (discrete) ensemble of independent harmonic oscillators. In the interaction term $\hat{\mathbf{d}}$ is the dipole operator associated with the emitter transition $|g\rangle\leftrightarrow|e\rangle$:

$$\hat{\mathbf{d}} = \mathbf{d}_{\mathrm{eg}}\hat{\sigma}_{+} + \mathbf{d}^{*}_{\mathrm{eg}}\hat{\sigma}_{-}, \tag{2.6}$$

with $\hat{\sigma}_{+} = |e\rangle\langle g|$ and $\hat{\sigma}_{-} = |g\rangle\langle e|$ the emitter raising and lowering operators, respectively. The matrix element $\mathbf{d}_{\mathrm{eg}} = \langle e|\hat{\mathbf{d}}|g\rangle$ is a possibly complex vector. We consider here a transition featuring a linear optical dipole and choose the phase reference such that $\mathbf{d}_{\mathrm{eg}} = d_{\mathrm{eg}}\mathbf{e}_d$, with d_{eg} a real positive number and $\mathbf{e}_d$ a unit vector. All emitter positions are equivalent in a uniform environment, we can thus set $\mathbf{r}_{\mathrm{em}} = \mathbf{0}$. The total electric field operator at this location is

$$\hat{\mathbf{E}}(\mathbf{0}) = \sum_{\mathbf{k},s}\hat{\mathbf{E}}_{\mathbf{k}s}(\mathbf{0}). \tag{2.7}$$

We next introduce the emitter-mode coupling strengths defined by

$$\hbar g_{\mathbf{k}s} = d_{\mathrm{eg}} \mathcal{E}_{\omega_{\mathbf{k}}} (\mathbf{e}_d \cdot \mathbf{e}_{\mathbf{k}s}). \tag{2.8}$$

With our phase convention, $g_{\mathbf{k}s}$ is a real number. The interaction term can be recast as

$$-\hat{\mathbf{d}} \cdot \hat{\mathbf{E}}(\mathbf{0}) = -i\hbar \sum_{\mathbf{k},s} g_{\mathbf{k}s} (\hat{\sigma}_+ + \hat{\sigma}_-)(\hat{a}_{\mathbf{k}s} - \hat{a}^\dagger_{\mathbf{k}s}). \tag{2.9}$$

As expected, $g_{\mathbf{k}s}$ strongly depends on the orientation of the mode polarization relative to the one of the emitter dipole. One may be worried that $g_{\mathbf{k}s} \propto 1/\sqrt{L^3}$ becomes vanishingly small in the large box limit ($L \to \infty$). As shown in the next section, this effect is exactly counterbalanced by an increase in the spectral density of modes, which yields a SE rate that does not depend on L.

2.3.3 A first approach: Fermi Golden rule

Our starting point is an excited emitter in the dark. The emitter-field system is initially in the discrete state $|e, 0\rangle = |e\rangle \otimes |0\rangle$, where $|0\rangle$ is the electromagnetic vacuum. The final state belongs to a continuum of states of the form $|g, 1_{\mathbf{k}s}\rangle = |g\rangle \otimes |1_{\mathbf{k}s}\rangle$, where $|1_{\mathbf{k}s}\rangle$ corresponds to 1 photon in mode $\{\mathbf{k}, s\}$ whereas all other modes are empty. The light-matter interaction governed by $\hat{H}_{\mathrm{int}}$ drives the "disintegration" of the discrete state $|e, 0\rangle$, which is eventually "diluted" into the continuum of final states $|g, 1_{\mathbf{k}s}\rangle$. Along the process, the population of $|e, 0\rangle$ decays in time according to an exponential law $\propto \exp(-\Gamma_0 t)$.

The SE decay rate Γ_0 can be calculated with a simple approach based on the Fermi Golden rule:

$$\Gamma_0 = \frac{2\pi}{\hbar^2} \sum_{\mathbf{k},s} |\langle g, 1_{\mathbf{k}s}| - \hat{\mathbf{d}} \cdot \hat{\mathbf{E}}(\mathbf{0}) |e, 0\rangle|^2 \delta(\omega_{\mathbf{k}} - \omega_{\mathrm{eg}}), \tag{2.10}$$

with $|\langle g, 1_{\mathbf{k}s}| - \hat{\mathbf{d}}.\hat{\mathbf{E}}(\mathbf{0}) |e, 0\rangle|^2 = d^2_{\mathrm{eg}} \mathcal{E}^2_{\omega_{\mathbf{k}}} (\mathbf{e}_d \cdot \mathbf{e}_{\mathbf{k}s})^2$. To proceed, we switch to a continuous summation using the equivalence rule $\sum_{\mathbf{k}} \leftrightarrow \left(\frac{L}{2\pi}\right)^3 \int\int\int \mathrm{d}^3\mathbf{k}$. After a few calculations, one obtains

$$\Gamma_0 = \left(\frac{2\pi}{\hbar^2}\right) \frac{2}{3} d^2_{\mathrm{eg}} \mathcal{E}^2_{\omega_{\mathrm{eg}}} \rho_0(\omega_{\mathrm{eg}}), \tag{2.11}$$

where $\rho_0(\omega) = \sum_{\mathbf{k}} \delta(\omega_{\mathbf{k}} - \omega)$ is the spectral density of states, given by

$$\rho_0(\omega) = \frac{\omega^2 n^3 L^3}{2\pi^2 c^3}. \tag{2.12}$$

Electronic properties of semiconductor nanostructures: Symmetry, exchange, and correlation effects

3

Andrei Schliwa
Institute of Solid State Physics, Technical University Berlin, Berlin, Germany

3.1 Introduction

III–V-system nanostructures exhibit a wide range of electronic and optical properties. These properties can be classified based on growth mode (Stranski-Krastanow or droplet etching), lattice structure (zinc-blende or wurtzite), carrier confinement type (I or II), confinement strength (weak, intermediate, strong, or hybrid), bandgap size (small to large), transition type (*k*-direct or *k*-indirect), growth planes (e.g., (100) or (111) for zinc blende, *c*/*m*/*a*-plane for wurtzite), and polarity (gallium vs. nitrogen polar [1, 2] in GaN *c*-plane).

To mention a few examples:

- Lattice-matched systems such as AlGaAs/GaAs [3, 4] or AlGaSb/GaSb [5] fabricated by epitaxially filling of nanoholes in an AlGaAs surface. The nanoholes are formed in a self-assembling fashion by local droplet etching.
- Highly strained small band direct semiconductors such as InGaAs/GaAs grown by Stranski-Krastanow growth [6, 7].
- Type II band-alignment occurs in case of GaSb/GaAs quantum dots (QDs) [8–11]: The confinement is attractive alone for holes but repulsive for electrons. If holes are present in the QD, eventually the band structure is modified to allow electrons be localized nearby at the interface by means of Coulomb interaction.
- GaP is the III–V binary compound with the nearest lattice constant to silicon [12] (0.37% lattice mismatch at room temperature) and—despite being an indirect semiconductor works well as a matrix for the $In_{1-x}Ga_xAs_ySb_{1-y}$ material combination [13–17].

Further examples will be examined more closely in this contribution by focusing on two cornerstones of current research: (i) InAs/GaAs(111)-plane and (ii) *c*-plane GaN/AlN QDs.

(i) For the past 20 years [18, 19], InAs/GaAs QDs have been a major area of research, leading to the creation of QD lasers [20] and single-photon emitters [21]. Due to the small bandgap of InAs, it is necessary to include valence band (VB) and conduction band (CB) coupling in electronic structure calculations. This has spurred the development of three-dimensional (3D) QD models beyond effective mass theory [22], with eight-band $\mathbf{k} \cdot \mathbf{p}$ theory being the most transparent [23]. As the search for single and entangled photon emitters continues,

Quantum Photonics. https://doi.org/10.1016/B978-0-323-98378-5.00004-0

the orientation of the substrate [24, 25] has become a crucial area of study, which will be discussed in this chapter.

(ii) The GaN/AlN material system [26–28] is of great interest due to three key differences from the previous systems: first, the state-of-the-art QDs are synthesized in the wurtzite phase instead of the zinc blende lattice. Second, GaN has a large bandgap, and third, GaN/AlN exhibits strong internal piezo- and pyroelectric fields. As we will see in Section 3.3.2, by varying the size of the GaN/AlN QDs, a large range of photon emission tunability from 2.6 to 4.5 eV can be achieved.

Both heterostructures belong to the III–V material system, and coherent growth is mediated by the sufficiently large lattice mismatch leading to QD formation in the Stranski-Krastanow growth mode [29]. The presence of strain alone can cause significant changes in the band structure and splitting of heavy hole (HH) and light hole (LH). Additionally, the lack of inversion symmetry and the inhomogeneous distribution of strain in III–V systems result in the generation of piezoelectric built-in fields.

The structure of the chapter is as follows: we begin by discussing the impact of lattice symmetries and Coulomb interaction on the electronic properties of QDs. Next, we provide details on the modeling method used in our research and present key findings. Finally, we focus on the single- and many-particle properties of InAs/GaAs (111)- and *c*-plane GaN/AlN QDs, with special emphasis on their excitonic and biexcitonic characteristics.

3.1.1 The role of lattice symmetries in zinc blende and wurtzite structures

Most QDs either carry zinc blende or wurtzite symmetry. In some cases, such as GaN, both allotropes are known to exist. The only difference between the zinc blende and wurtzite lattices is in their second-nearest neighbors (see Fig. 3.1b and c). These lattices can be described using different layer sequences, such as *AB AB AB A* (along the *c*-axis) or *ABC ABC A* (along the ⟨111⟩-axis), similar to the hexagonal and cubic close packing structures.

These minute differences between zinc blende and wurtzite crystals result in varying symmetry properties. Zinc blende crystals have four threefold axes of rotation

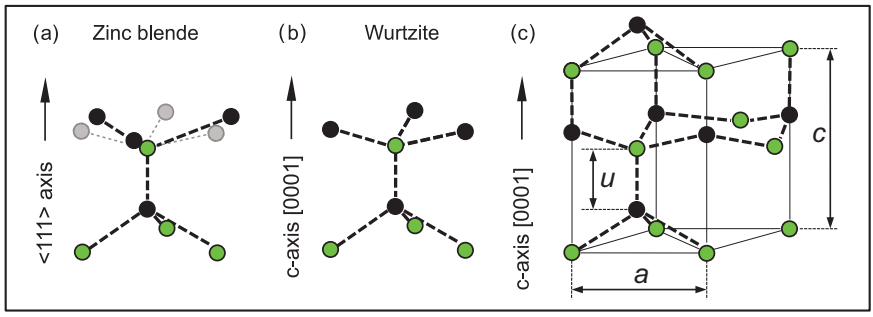

Fig. 3.1 (a, b) The differences in position of second nearest neighbors between zinc blende and wurtzite lattice are shown. (c) Wurtzite unit cell with lattice parameters *a* and *c* together with the internal (dimensionless) parameter *u*.

3.2.3.5 *Optical properties*

Interband spectra

The interband absorption spectra are calculated by Fermi's golden rule applied to excitonic states calculated by the CI method [80].

The decay of excitons is not governed by strict selection rules. As a general rule, transitions with large oscillator strength are those in which the electron and hole states have similar symmetry properties and a significant spatial overlap. However, since hole states consist of both HH and LH components (see Fig. 3.13), each with its own symmetry, they can recombine with a number of different electron states, visible in Fig. 3.15a1. In other words the symmetry properties of the electron and hole states are not the only determining factor in the decay of excitons.

Intraband spectra

In contrast to the excitonic decay the CB intraband transitions follow strict transition rules (see Fig. 3.14): for two electron states, $|a\rangle = |ijk\rangle$ and $|b\rangle = |i'j'k'\rangle$, it is a necessary condition that at least one of the expressions $i - i'$, $j - j'$, or $k - k'$ is an odd number. For example, the transition between the electron states $|100\rangle \rightarrow |000\rangle$ has a significant oscillator strength in contrast to $|200\rangle \rightarrow |000\rangle$, which is a forbidden transition. In general, the oscillator strength of intraband transitions is smaller than for

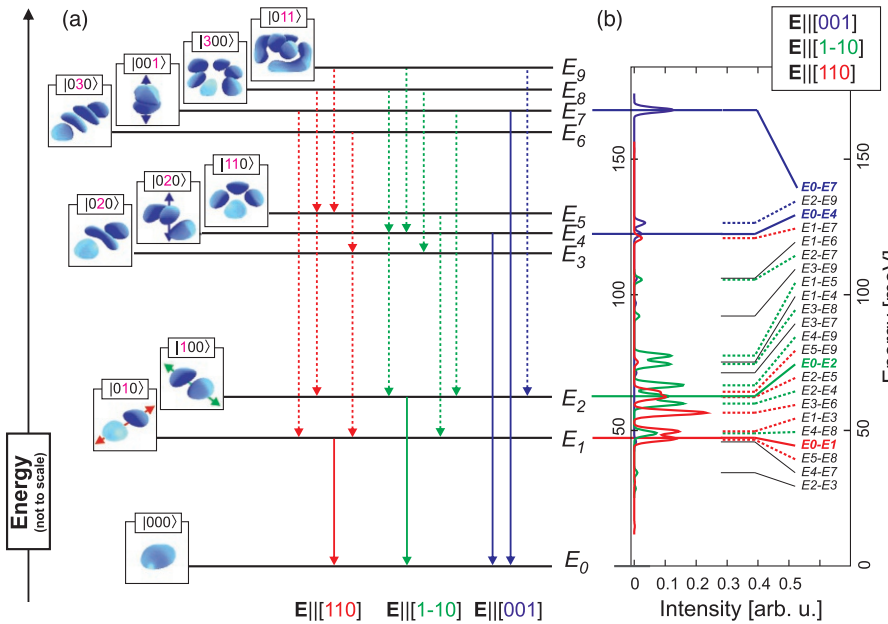

Fig. 3.14 The absence of strict selection rules in intraband transitions are shown for electronic wavefunctions in a pyramidal quantum dot. (a) Dominant transition paths for conduction band intraband transitions are marked with *solid lines*, weak with *dotted lines*. The corresponding transition spectra are shown in (b) for three polarization directions.

Cavity quantum electrodynamics and polaritons

4

The physics of exciton-polaritons

Sebastian Klembt, Simon Betzold, and Sven Höfling
Julius-Maximilians-Universität Würzburg, Physikalisches Institut and Würzburg-Dresden Cluster of Excellence ct.qmat, Lehrstuhl für Technische Physik, Am Hubland, Würzburg, Germany

4.1 Introduction

Exciton-polariton, or more precisely microcavity exciton-polaritons, are the new resulting eigenmodes of strong light-matter coupling of a quantum well (QW) exciton to a cavity photon mode in an optical microresonator [1]. Resulting from dominant absorption and reemission processes, new part-light part-matter quasiparticles are formed that we will simply call *polaritons* from here on. In contrast to cavity quantum electrodynamics with individual two-level systems such as atoms [2] or quantum dots [3], here, an ensemble of QW excitons couples collectively to the cavity mode. It has quickly become clear that the resulting new quasiparticles are composite bosons with a very light effective mass inherited from their light part. Thus polaritons have immediately attracted interest for experiments on Bose-Einstein condensation (BEC) at elevated temperatures. At the same time, their initial experimental observation by Weisbuch et al. in the Arakawa group in 1992 [1] was predicated on a more and more refined fabrication process of III–V semiconductor microcavities, as well as other material systems. These experimental platforms immediately opened this field toward the engineering of, for example, ultra-low threshold lasers and quantum simulators on a semiconductor chip, spanning a fascinating range from fundamental physics and correlated systems to applied semiconductor research. This chapter will attempt a concise introduction into polariton physics before highlighting and discussing current and exciting new aspects of this field.

To have a high probability for strong interactions between photons and excitons, one has to provide and engineer an efficient sample geometry to confine both to the smallest possible volume. Excitons are fundamental optical excitations where an electron is bound by Coulomb forces to a hole forming an electron-hole pair with the total energy of

$$E_X(\mathbf{k}, i) = E_g - E_{b,i} + \frac{\hbar^2 \mathbf{k}^2}{2m_{X,eff}},$$

where E_g is the bandgap energy, $E_{b,i}$ is the binding energy of ith excitation, and the kinetic term describing the motion of an exciton by assigning an effective exciton

Quantum Photonics. https://doi.org/10.1016/B978-0-323-98378-5.00005-2

modes, where the energetic separation of the modes is a measure for the strength of the coupling [156]. Fig. 4.16E shows energy-resolved real-space emission measurements of photonic molecules with different ratio v. The diameter of each hemisphere was 5 μm and the effective radius of curvature was 25 μm. For a ratio of $v = 0.6$, that is, for a center-to-center distance of 3 μm, several dispersionless modes in the energy range between 1.85 and 1.95 eV can be recorded. For the two low-energy modes, no coupling can be detected, but only two spatially separated s modes. The two energetically higher modes, on the other hand, can be assigned to the binding and antibinding p_x modes. As expected, the p_y modes are not visible in the spectrum due to a node of the electric field for $y = 0$. Finally, for a v of 0.5, a splitting into binding and antibinding s modes can be resolved. In addition the coupling of the p_x modes increased due to the stronger overlap, which is evident from the larger energetic distance. For decreasing center distances, the splittings of the binding and antibinding modes increase further accordingly. As expected, this is true for both the s modes and the p_x modes. For a more detailed analysis of the mode structure of the hybridized s and p modes, the already introduced method of mode tomography was used on the molecule with $v = 0.4$. Fig. 4.16F shows spatially resolved energy slices of the hybridized s and p modes (in each case on the right, experiment). In addition, hybrid modes calculated by the linear combination of modes method are shown in the figure. The experimental results and the calculations show very good agreement with respect to the mode shape and, in addition to the energetic position, the hybrid modes could be unambiguously assigned.

4.5.3.2 1D and 2D lattices

The high quality of the microcavities as well as the excellent control over the coupling allowed the next step toward the controlled confinement of polaritons in more complex potential landscapes, as shown in Fig. 4.17A. In 2020, the Würzburg group

Fig. 4.16 Single traps and polaritonic molecules as building blocks for polaritonic lattices. (A) Schematic of the tunable Gaussian defect microcavity, real-space images of Laguerre Gaussian and planar modes, and angle-resolved photoluminescence measurements. (B) Atomic force microscopy image of the fabricated top part of the cavity with a closely Gaussian defects (*left*). The coupling splits the LG00 mode into a bonding (LG00B) and an antibonding (LG00AB) mode. Real-space mode patterns (*center*) and angle-resolved photoluminescence of the coupled Gaussian structure (*right*). (C) Angle-resolved emission measurement of a hemispherical microcavity with a radius of curvature of $R = 16$μm. Dispersion-less modes formed due to the confinement potential are clearly visible up to a transverse mode order of at least five (*left*). Hyperspectral imaging measured and composite energy sections of the transverse modes shown on the left up to mode order $m = 5$. (D) Real-space emission spectra of polaritonic molecules for different center-to-center distances. (E) Spatially resolved iso-energy cuts of a mode tomography of the polaritonic molecule with $v = 0.4$ together with calculated hybrid modes.
(A, B) From D. Urbonas, T. Stöferle, F. Scafirimuto, U. Scherf, R.F. Mahrt, ACS Photonics 3 (2016) 9; (C–E) From S. Betzold, Starke Licht-Materie-Wechselwirkung und Polaritonkondensation in hemisphärischen Mikrokavitäten mit eingebetteten organischen Halbleitern (Ph.D. thesis), 2022, https://doi.org/10.25972/OPUS-26665.

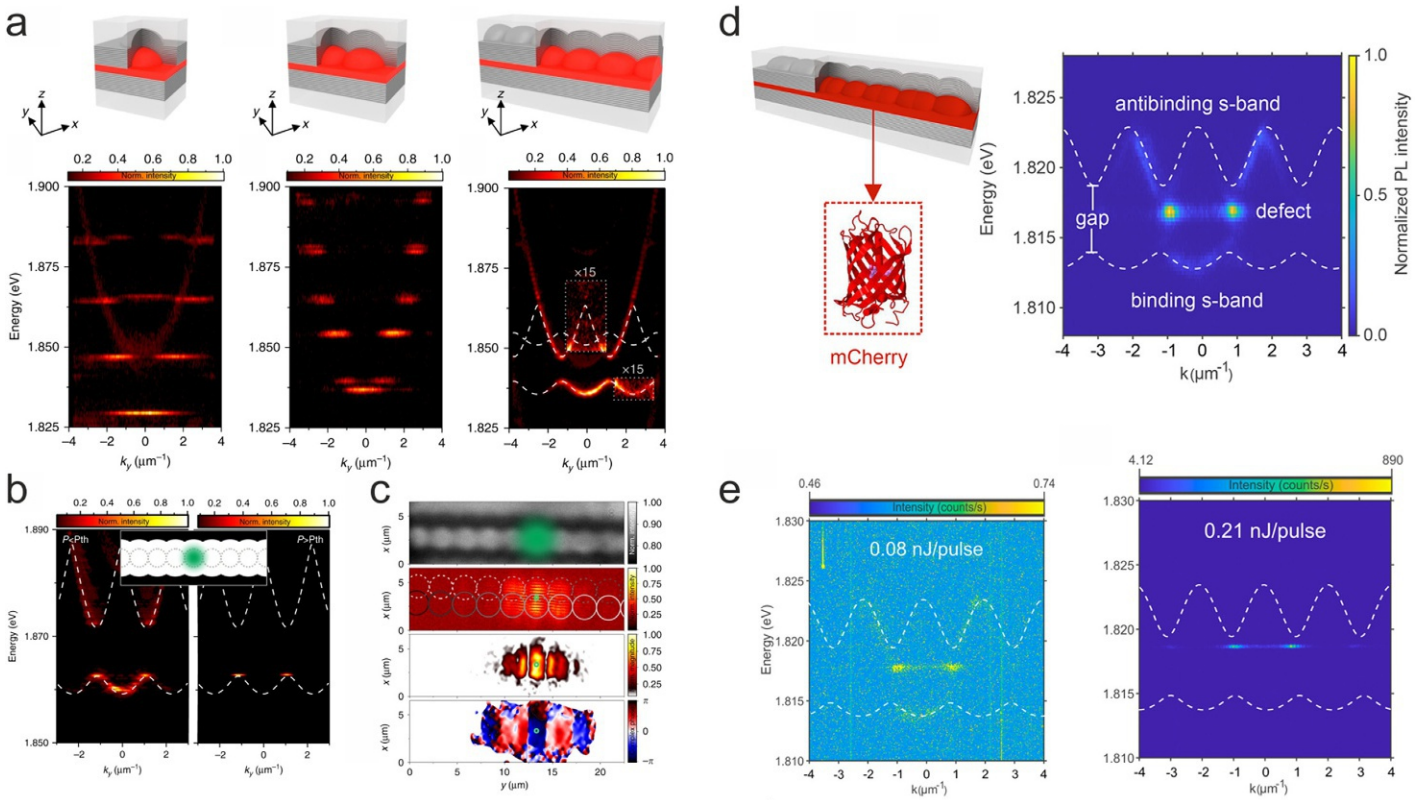

Fig. 4.17 Polariton lasing in one-dimensional organic lattices. (A) Angle-resolved spectra of a single lens, a molecule, and a linear 1D lattice, and corresponding schematic illustrations. (B) Angle-resolved measurement below (*left*) and above (*right*) the polariton lasing threshold. (C) Interference measurements and extracted visibility and phase on the linear chain. (D) *Left*: Schematic depiction of a linear 1D SSH chain microcavity. *Right*: Angle-resolved measurement in the domain boundary defect region. A topological gap of ≈4.9 meV opened, in which a defect mode is located. (E) Excitation power-dependent and angle-resolved measurements show the transition to the polariton condensate for the domain boundary mode.
(A–C) From M. Dusel, et al., Room temperature organic exciton-polariton condensate in a lattice, Nat. Commun. 11 (2020) 2863; (D, E) From M. Dusel, et al., Room-temperature topological polariton laser in an organic lattice, Nano Lett. 21 (2021) 6398–6405.

Semiconductor quantum dot lasers: Genesis, prospects, and challenges

5

Frédéric Grillot[a,b], *Jianan Duan*[c], *Bozhang Dong*[d], *and Heming Huang*[a]
[a]Télécom Paris, Institut Polytechnique de Paris, Palaiseau, France, [b]Center for High Technology Material, University of New Mexico, Albuquerque, NM, United States, [c]School of Electronic and Information Engineering, Harbin Institute of Technology, Shenzhen, China, [d]Institute for Energy Efficiency, University of California Santa Barbara, Santa Barbara, CA, United States

5.1 Introduction

Over the past few decades, our daily lives have been reshaped by the emergence of new technologies. The popularization of smartphones, for example, has radically transformed our daily routine and the associated industries. Today, a wide variety of online services based on cloud computing and cluster analysis are at our fingertips. Moreover, with the ongoing construction of the Internet of Things (IoT), or the more ambitious Internet of Everything (IoE), billions of devices and sensors are connected to the network each year, hence generating real-time feedback for various monitoring purposes [1]. In addition to IoT/IoE, artificial intelligence and machine learning are booming and continuously launching more innovative applications in education, healthcare, and transportation, to name a few. As a result, global data traffic is growing every year, reaching 5 zettabytes (ZB) per month on mobile networks alone by the end of 2030, according to the recent estimates from the International Telecommunication Union [2]. At the same time, the communication infrastructure is constantly being upgraded, especially at its core, the optical layer, to accommodate the rapid growth in Internet use, which has increased at least 16-fold by 2020 compared with 2010, as reported by the International Energy Agency [3]. High-speed, low-latency optical links are among the most in-demand equipment to meet transmission capacity requirements, especially in access networks and very large-scale data centers. By 2026, the global optical transceiver market is expected to double to approximately $21 billion [4].

Currently, common optical transceivers include a semiconductor laser light source, a modulator, a (de)multiplexer, and a photodetector, all assembled around a printed circuit board (PCB). The heat generated by the electronic components can easily jeopardize stability and performance, as semiconductor lasers are generally strongly sensitive to thermal issues. In addition, the functionality of edge emitters is rather

Quantum Photonics. https://doi.org/10.1016/B978-0-323-98378-5.00008-8

academics and industries. In 2008, the first QD laser directly developed on silicon operating at 1.3 μm was introduced by Arakawa's group [163]. Following this significant development, resources are pooled into improving the epitaxy growth [157, 164, 165]. Before long, TD interference has been largely reduced [20], pushing the QD device performance at the height and even beyond that of the native substrate level mostly with MBE [143], and more recently by demonstrating a fully CMOS-compatible silicon approach by MOCVD direct heteroepitaxy, the latter being inferred more desirable for high-volume production [166]. Very recently, novel QD and QDash material systems have also been demonstrated for silicon integration [167–170], bringing more optical functionalities on to Si platform, and unleashing even more potential of silicon photonics into industrial applications [171]. In this context, Tower Semiconductor and Quintessent also announced a partnership to create a foundry silicon photonics platform with integrated QD Lasers [172].

Moreover, the insensitivity of QD lasers against external reflection offers a workaround to the optical feedback issue in photonic integration. Usually, there are many interfaces on a PIC chip, for example, between different materials, between building blocks, as well as from the passive and active interfaces/transition; all can potentially generate unwanted parasitic reflections that would destabilize the laser and render the optical signal transmission inoperable. Up to date, there are still no low-cost and efficient solutions to incorporate an optical isolator to overcome such obstacle. QD lasers, however, inheriting excellent feedback resistance can resist high amount of optical reflections [173] and operate without an optical isolator [23].

5.3 Noise properties of quantum dot lasers

Low noise semiconductor lasers are required in many areas such as high-performance coherent communications [174], radio-frequency (RF) photonics [175], optical atomic clock [176], frequency synthesis [177], spectroscopy [178], and distributed sensing systems [179]. In semiconductor lasers, quantum fluctuations alter both intensity and phase of the optical field, hence leading to frequency and intensity noises [180]. The frequency noise (FN) determines the spectral linewidth of the laser. Apart from the FN, the optical sources with low relative intensity noise (RIN) are highly desired not only for optical communication systems, but also for radar-related applications. This section highlights the narrow linewidth and low RIN operation of QD lasers.

5.3.1 Spectral linewidth

The FN in semiconductor lasers results from low-frequency flicker noise, spontaneous emission noise, as well as carrier generation and recombination noise. The flicker noise arises from current source, thermal fluctuations, and internal electrical noise. The remaining noise sources are white noise and govern the intrinsic spectral linewidth of the laser, which is fundamentally driven by a phase diffusion process contributed from both spontaneous emission and phase-amplitude coupling effect. Fig. 5.3 schematically illustrates the phase-amplitude coupling effect on the phase

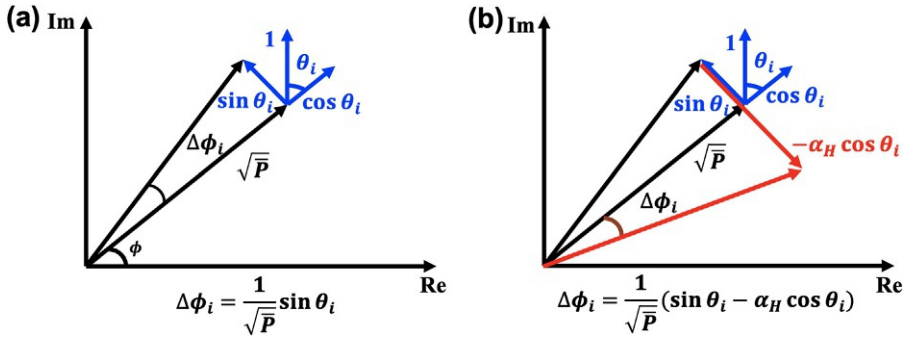

Fig. 5.3 Schematic comparison of the phase diffusion ($\Delta\phi_i$) of the lasing field between direct action of the spontaneous emission events only (A) and joint action of both spontaneous emission events and phase-amplitude coupling (B). The corresponding phase change for each case is indicated by the relationship, where the amplitude and the phase of the lasing field are denoted by $\sqrt{\bar{P}}$ and ϕ, respectively.

diffusion of the lasing field. The linewidth enhancement factor (α_H-factor) is associated with the interaction between the intensity and phase of the lasing field and is used to quantitatively describe the phase-amplitude coupling effect. The spectral linewidth of semiconductor lasers is expressed by the modified Schawlow-Townes expression [181]:

$$\Delta\nu = \frac{\Gamma g_{th}\nu_g^2\alpha_m h\nu}{4\pi P_0} n_{sp}(1+\alpha_H^2) \tag{5.4}$$

where Γg_{th} is the threshold modal gain, α_m is the transmission loss, $h\nu$ is the photon energy, P_0 is the optical output power, n_{sp} is the population inversion factor, and ν_g is the group velocity. For a Fabry-Pérot resonator, the α_m can be expressed as

$$\alpha_m = \frac{1}{2L}\ln\left(\frac{1}{R_1R_2}\right) \tag{5.5}$$

where L is the cavity length, and R_1 and R_2 are the power facet reflectivity. From Eq. (5.4), the spectral linewidth can be reduced not only by decreasing the α_m or the α_H-factor, but also by increasing the output power P_0. The decrease of the α_m can be achieved by means of increasing the cavity length or the facet reflectivity. An example is a fully integrated extended distributed Bragg reflector (DBR) laser with ~1 kHz linewidth and a ring-assisted DBR laser with less than 500 Hz linewidth [182, 183].

Furthermore, the definition of the spectral linewidth can be equivalently reexpressed in terms of quality factor by [184]

$$\Delta\nu = \frac{\pi h\nu^3}{QQ_{ext}\eta_d(I-I_{th})} n_{sp}(1+\alpha_H^2) \tag{5.6}$$

Semiconductor quantum dot based quantum light sources

6

Sven Rodt[a], *Hüseyin Vural*[b], *Simone Luca Portalupi*[b], *Peter Michler*[b], *and Stephan Reitzenstein*[a]
[a]Institute of Solid State Physics, Technical University of Berlin, Berlin, Germany, [b]Institute of Semiconductor Optics and Functional Interfaces, University of Stuttgart, Stuttgart, Germany

6.1 Introduction

Semiconductor quantum dots (QDs) are nanocrystals with excellent optical and quantum optical properties. They are formed by self-assembled epitaxial growth of semiconductor heterostructures with different band gap energies and different lattice constants [1–5]. Stress relaxation leads to quasi-zero-dimensional nanostructures, the QDs, with discrete electronic energy levels that can act as near-ideal two- and three-level systems [6, 7]. This explains the great interest in single QDs as active elements of quantum photonic devices [8–13]. In fact, QDs can function as nanophotonic turnstile devices, emitting one and only one photon upon an optical or electronic trigger event [14]. In this sense, and in contrast to nondeterministic sources based on attenuated lasers or parametric down-conversion, QDs are ideal quantum emitters, capable of delivering single photons on demand, which is highly interesting for applications of photonic quantum technologies. Noteworthy, since single photons are the primary information carriers in quantum networks [15, 16], QDs in quantum photonics receive a similar attention as semiconductor lasers in classical photonics, where information is usually carried by a large number of millions of photons. However, individual QDs themselves are not practical single-photon sources since their emission is nondirectional and total internal reflection at the semiconductor-air interface further reduces the number of usable photons in external collection optics to a few percent at most [17]. For this reason, tremendous efforts worldwide have been directed toward the development and realization of nanophotonic devices that maximize the photon-extraction efficiency of QDs [12, 18]. In this context, micro- and nanocavities are of particular interest as they apply cavity quantum electrodynamics (cQED) concepts to boost the emission of individual QDs and direct generated photons into the target collection optics, which is the first lens of a quantum photonics setup or an optical fiber when it comes to practical plug'n'play devices that can be used directly in quantum networks.

The controlled fabrication of such quantum devices with high process yield and best possible performance is a major challenge owing to the self-organized growth of QDs, which leads to random nucleation sites and a highly inhomogeneous distribution of emission wavelengths within a QD ensemble (Fig. 6.1) [1, 19].

Quantum Photonics. https://doi.org/10.1016/B978-0-323-98378-5.00006-4

despite position control, spectral resonance per se is still not guaranteed in the manufacturing process, and postprocessing schemes such as strain tuning are required to ensure optimum device performance. The existing device concepts for QD QLS (see Section 6.3) have in common that the quantum emitter has to be integrated into the active region with nm precision (or a few tens of nm) to ensure the best possible performance, for example, in terms of photon-extraction efficiency. In addition, in cavity-enhanced devices, spectral resonance between the emitter and the cavity mode must be ensured. To achieve a reliable control of the coupling between photonic structure and randomly distributed emitters, different deterministic fabrication technologies have been developed. While the following text focuses on QDs as testbed, this technique can be extended to other kinds of quantum emitters.

To overcome the mentioned problem, several deterministic nanofabrication technologies have been developed in recent years. They essentially include pick-and-place techniques [63, 100–105] as well as marker-based [106–109] and in situ lithography techniques [26, 27, 29, 75, 110] (Fig. 6.7). The approaches can be distinguished that, in the case of pick-and-place techniques, the QD structures are picked-up (e.g., in case of dots in a wire) or patterned using regular EBL before suitable devices are selected for integration into, e.g., photonic quantum circuits. In contrast, for marker-based and in situ lithography techniques, the emitter is selected first and in the second step, the target nanophotonic structure such as a micropillar cavity is written by optical lithography or EBL to ensure spatial and spectral resonance with the selected emitter.

6.5.1 Pick-and-place fabrication technology

A great benefit of pick-and-place techniques is the separation of the growth (and patterning) of the (QD-based) emitting structure and the (nano) photonic environment. Consequently, structures within the same material system or of different material systems can be combined. The latter ones are called hybrid systems. Prominent examples are QD structures that are attached (in-) to low-loss silicon-based waveguide circuits like InAs QDs in InP nanobeams [101], InAsP QDs in InP nanowires [63, 102], InAs QDs in tapered GaAs waveguides [103], and InAs QDs in GaAs nanobeam cavities [105]. Another hybrid system constitutes of a GaAs photonic wire with a single InAs QD inside that is attached onto the facet of an optical fiber [100]. A combination of the pick-and-place technique with deterministic in situ EBL can be found in [104] where a tapered GaAs waveguide with a deterministically integrated InGaAs QD was positioned on top of a silicon-based waveguide that enabled the emission of indistinguishable photons. For the sake of completeness and to go beyond QD-based light sources, it should be mentioned that diamond-based QLS, like single NV centers in nanodiamonds, are attractive candidates for pick-and-place assemblies [111], too.

Besides the possibility to combine different material platforms, an advantage of the pick-and-place technique is that the design of integrated photonic circuits can be optimized without considering the (random) position of the QD nanophotonic structure, which will be placed on the optimum position after the circuit fabrication by a nanomanipulator. However, the latter process is cumbersome, which again limits the scalability and practicality of this deterministic fabrication technique.

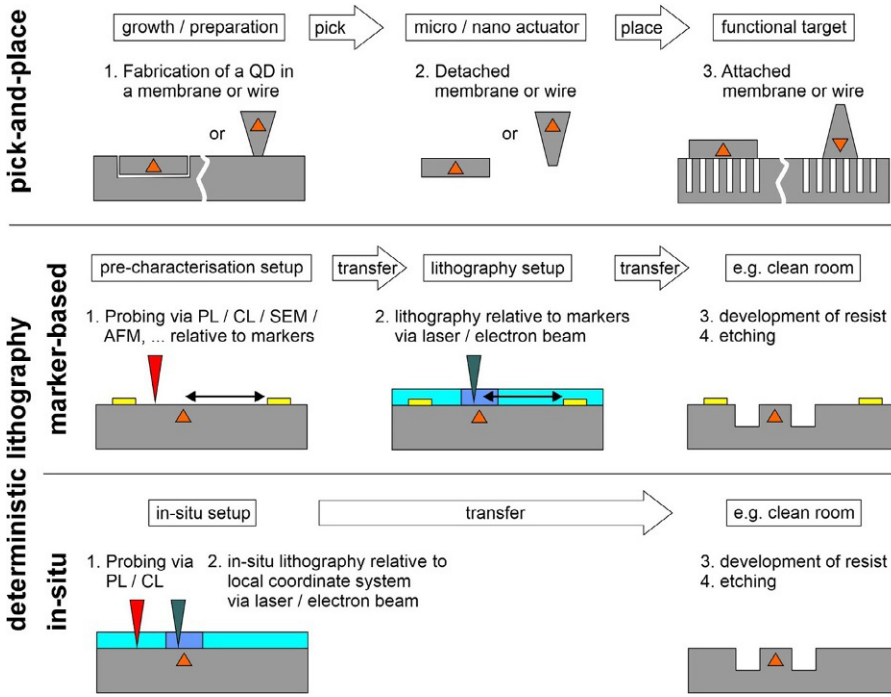

Fig. 6.7 Sketch of deterministic QLS fabrication techniques. *Top*: The pick-and-place technique relies on preprocessed semiconductor objects with single QDs inside that are mechanically transferred to nanophotonic structures. *Middle* and *bottom*: Deterministic lithography techniques that utilize marker structures to relocate single QDs in different setups for spectroscopy and lithography and that perform an in situ process in which preselection and lithography are performed in one and the same setup to avoid error-prone coordinate matching and simplify the process for, e.g., future automated QLS fabrication.
Extension of fig. 8.6 in S. Rodt, P.-I. Schneider, L. Zschiedrich, T. Heindel, S. Bounouar, M. Kantner, T. Koprucki, U. Bandelow, S. Burger, S. Reitzenstein, Semiconductor Nanophotonics, Springer International Publishing, 2020 (Chapter 8) p. 285ff, https://doi.org/10.1007/978-3-030-35656-9.

6.5.2 Deterministic optical lithography

As introduced in the previous paragraph, the most widely used semiconductor QDs are deposited via processes that result in the emitter's random spatial distribution. Furthermore, the self-assembled growth process results in the observation of an inhomogeneously broadened emission wavelength distribution from the QD ensemble. This poses a challenge when cQED effects are to be employed since they require the spatial match of the emitter with respect to the maximum of the cavity electromagnetic mode, as well as the spectral matching between the QD transition and the resonator frequencies. While several experimental studies were (and are still) based on the possibility to fulfill spatial and spectral matching conditions with a statistical approach (i.e., creating arrays of resonators on the sample), high device yield and

Quantum light sources based on color centers in diamond and silicon carbide

7

Norikazu Mizuochi[a,b] *and Naoya Morioka*[a,b]
[a]Institute for Chemical Research, Kyoto University, Uji, Japan, [b]Center for Spintronics Research Network, Institute for Chemical Research, Kyoto University, Uji, Japan

7.1 Spin-active quantum light sources in diamond

7.1.1 Introduction

Recently, there has been high interest in diamond and silicon carbide (SiC) color centers as important physical systems for emergent quantum technologies, including quantum metrology, information processing, and communications, as well as for various nanotechnologies and biological imaging. Particularly, quantum light sources are one of the most important applications.

Among the color centers in diamond, nitrogen-vacancy (NV) centers are the most interesting ones. Historically, the NV center were eagerly investigated in the 1970s due to interest in the origin of diamond's color, because optical absorption between electronic states created by impurity defects in the bandgap determined the color of diamond. The atomic structure, which is shown in Fig. 7.1A, was revealed by optical [1] and electron spin resonance (ESR) [2] techniques. In 1997, a single NV center was observed by confocal microscopy at room temperature. Furthermore, the single NV center's single spin was also measured by optically detected magnetic resonance (ODMR) technique [3]. The background to this success at the time was the development of measurement techniques of single molecule observation [4,5]. The observation of the single NV center triggered research of not only the NV center but also the other color centers in diamond and SiC in the field of quantum information science. In 2000, it was shown that the fluorescent light of the single NV center exhibits photon antibunching [6]. The potential of a stable solid-state source of a single photon was demonstrated from its robustness against photobleaching and the simplicity of the all-solid-state setup. Regarding control of the spin, the electron spin can be optically initialized, and Rabi oscillations of electron and nuclear spins of the single NV centers were demonstrated at room temperature [7,8]. The spin property of the NV center is excellent, and the coherence times of the NV center's electron spin are the longest among those in the solid-state qubit [9]. In 2008, using the coupling with nuclear spins near the NV center, we demonstrated the generation of quantum entanglement states, the so-called Bell state and Greenberger-Horne-Zeilinger (GHZ) state [10]. After that, using quantum entanglement between photons and spins, the generation of quantum

Quantum Photonics. https://doi.org/10.1016/B978-0-323-98378-5.00009-X

7.2.2.1 Optical and spin properties

We here focus on negatively charged Si vacancies in 4H-SiC, which have been studied intensively as quantum light sources. Fig. 7.4A shows the structure of a Si vacancy (V1) in 4H-SiC. V_{Si}^{-} belongs to the point group C_{3v} and has a slight distortion from tetrahedral symmetry. The energy-level diagram for V_{Si}^{-} is depicted in Fig. 7.4B. The ground state is $^4A_2$, and the first and second electronic excited states are $^4A_2$ and ^4E, respectively. Note that the excited states are not pure electronic states; the $^4A_2$ and ^4E states are mixed because of phonons and form polaronic states [114]. The zero-field splitting for the ground state is $2D_{gs} = 4.5 \pm 0.3$ MHz [97] and 69.99 ± 0.03 MHz [109] for V1 and V2, respectively. The D_{gs} for V2 is almost temperature independent from cryogenic temperatures to 500 K [114–116]. However, the excited-state zero-field splitting D_{es} is strongly temperature dependent: $2D_{es} = 1$ GHz for both V1 and V2 at cryogenic temperatures and becomes smaller at higher

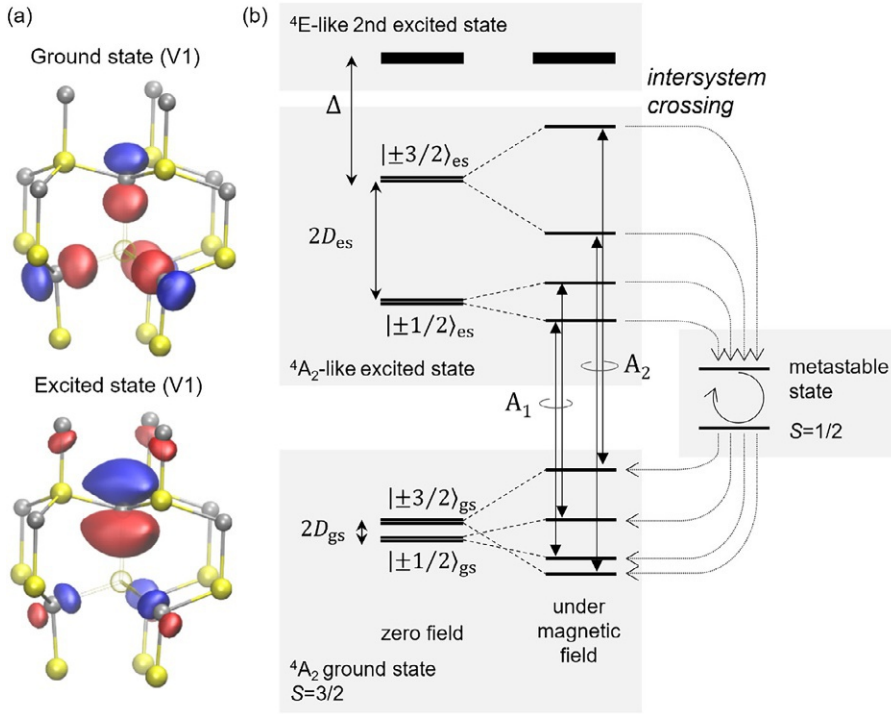

Fig. 7.4 Negatively charged Si vacancy in 4H-SiC. (A) Structure and electronic wavefunction of the ground and excited states of the V1 center. (B) Energy-level diagram for Si vacancy. (A) From R. Nagy, M. Niethammer, M. Widmann, Y.-C. Chen, P. Udvarhelyi, C. Bonato, J.U. Hassan, R. Karhu, I.G. Ivanov, N.T. Son, J.R. Maze, T. Ohshima, Ö.O. Soykal, Á. Gali, S.-Y. Lee, F. Kaiser, J. Wrachtrup, High-fidelity spin and optical control of single silicon-vacancy centres in silicon carbide, Nat. Commun. 10 (1) (2019) 1954, reproduced under the Creative Commons License CC-BY 4.0 (http://creativecommons.org/licenses/by/4.0/).

Atom-based photonics

8

Takao Aoki
Department of Applied Physics, Waseda University, Shinjuku-ku, Tokyo, Japan

8.1 Introduction

Atoms are indispensable elements in quantum photonics, and the interaction of atoms and light offers a variety of useful quantum-photonic functions. An atom can absorb or emit only one photon at a time through its electronic transition because of the unharmonic nature of the Coulomb potential. Therefore, an atom is an ideal source of single photons. The unharmonicity of the Coulomb potential also yields strong optical nonlinearity at the single-photon level, and this can be utilized for quantum gates. Dissipations can be reduced and the atomic states with long coherence times can be utilized for quantum memories when the atoms are laser cooled and trapped in vacuum. The performance of these quantum photonic functions can be enhanced by using high-finesse cavities or nanophotonic structures that can confine light in small volumes and enhance atom-light interactions. A large-scale quantum network can be constructed by combining these functions [1–5]. In this chapter, we focus on laser-cooled atoms (mainly neutral atoms, with some reference to ions) and review their applications in quantum photonics.

8.2 Single atoms in free space

The absorption cross-section of an atom is given by

$$\sigma = \frac{3\lambda_{\mathrm{A}}^2}{2\pi}, \tag{8.1}$$

where $\lambda_{\mathrm{A}} = 2\pi c/\omega_{\mathrm{A}}$, ω_{A}, and c denote the resonance wavelength of the atom, resonance frequency of the atom, and speed of light, respectively (Fig. 8.1A). Therefore, an atom interacts only weakly with a light beam in free space with a radius larger than the wavelength. A simple workaround for this is the use of an ensemble of many atoms. Dense clouds of atoms can be created using magneto-optical traps [6], which are useful platforms for quantum memories. However, an atom interacts appreciably with a light beam tightly focused on a beam area compared to σ at the position of the atom (Fig. 8.1B); this can be achieved using a single lens with a large numerical aperture (NA) because the beam waist radius w_0 is given by $\lambda/(\pi NA)$, where λ represents the wavelength of the beam. Indeed, the extinction of a resonant light beam close to 10% was observed by focusing the beam with a single lens [7].

Quantum Photonics. https://doi.org/10.1016/B978-0-323-98378-5.00013-1

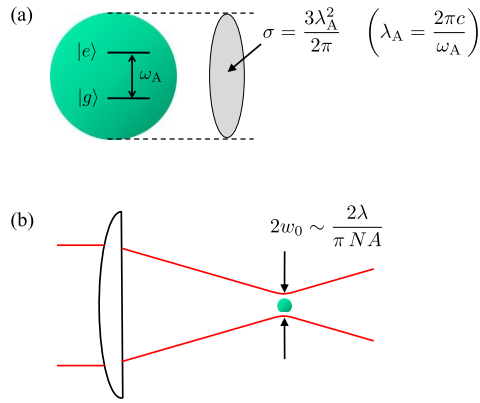

Fig. 8.1 (A) Absorption cross-section of an atom. (B) Focusing on a light beam using a lens.

An atom absorbs or emits only one photon at a time by its electronic transition because of the unharmonic nature of the Coulomb potential; this makes an atom an ideal source of single photons. The unharmonicity of the Coulomb potential also yields strong optical nonlinearity at the single-photon level [8] and a pronounced modification of photon statistics [9, 10].

Only one atom is trapped instead of an ensemble of multiple atoms to exploit these properties. This is realized using an optical dipole trap [11], a far-off resonant trap (FORT) with a tightly focused beam, or an optical microtrap [12, 13]. Strong light-assisted two-body collisions occur when multiple atoms are loaded into a microtrap and illuminated by near-resonant light, and only one or no atoms are left in the trap; this mechanism is known as "collisional blockade" [14]. It is preferable to cool the atom in the trap because the thermal motion of the atom causes unwanted effects such as dynamic light shifts. Raman sideband cooling is a powerful method for cooling atoms in microtraps close to its three-dimensional ground state [15, 16].

Further, it is possible to create multiple microtraps, each of which has a single atom, and to move their positions while preserving the coherence of the trapped atoms [17]. Two-particle quantum interference of atoms has been observed [18], and the entanglement between two transportable atoms has been created using such methods [19]. In addition, it is possible to create approximately 100 microtraps with individual control using acousto-optical deflectors and spatial light modulators; defect-free arrays of trapped atoms in one [20], two [21], and three [22] dimensions have already been created.

In contrast to neutral atoms, ions repel each other because of Coulomb repulsion. In the linear radio-frequency quadrupole trap (Paul trap), ions form a one-dimensional array because of the harmonic confinement of the trap and the mutual Coulomb repulsion [23, 24]. Typical separations between neighboring ions are a few microns, and each ion can be individually observed or manipulated using a lens with a decent NA [25].

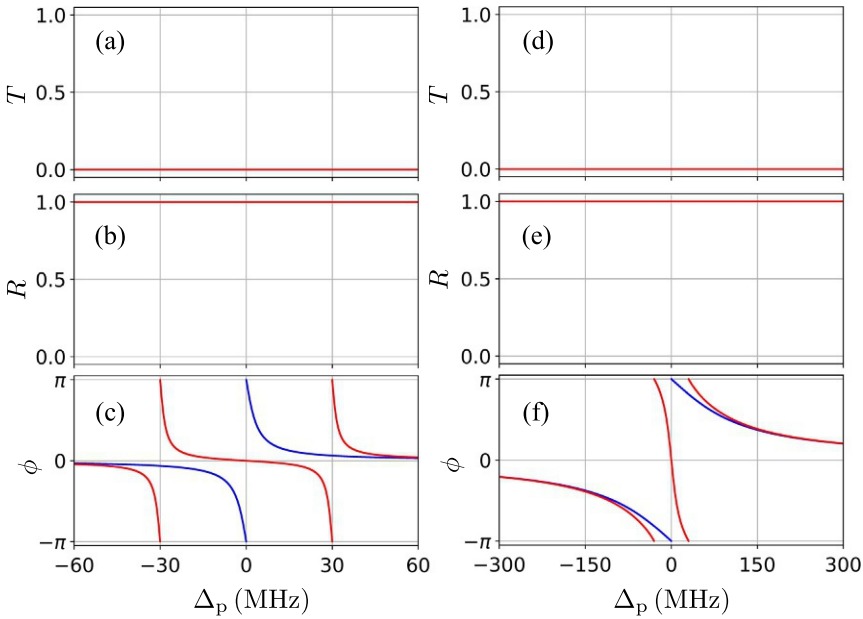

Fig. 8.4 Optical responses of a cavity QED system in the weak-driving limit for ideal cases. The *red* and *blue lines* represent the cases with and without an atom, respectively. The cavity QED parameters are $(g, \kappa_{1,\mathrm{ex}}, \kappa_{2,\mathrm{ex}}, \kappa_{\mathrm{in}}, \gamma) = 2\pi \times (30, 3.0, 0, 0, 0)$ MHz for (a), (b), and (c) (strong coupling regime), and $(g, \kappa_{1,\mathrm{ex}}, \kappa_{2,\mathrm{ex}}, \kappa_{\mathrm{in}}, \gamma) = 2\pi \times (30, 100, 0, 0, 0)$ MHz for (d), (e), and (f) (Purcell regime).

8.3.5 Λ-type three-level atom

A cavity QED system with a Λ-type three-level atom instead of a two-level atom offers an even greater variety of functions. As shown in Fig. 8.5, the atom has one excited state, $|e\rangle$, and two stable ground states, $|g\rangle$ and $|u\rangle$. The transition $|g\rangle \leftrightarrow |e\rangle$ is coupled to the cavity at a rate of g, which is the same as in the two-level atom case. In contrast, the transition $|u\rangle \leftrightarrow |e\rangle$ is not coupled to the cavity; however, it can be driven by an external field (e.g., by illuminating a laser beam from the side of the cavity). The Hamiltonian for this system can be written by extending the Jaynes-Cummings Hamiltonian to the three-level atom as

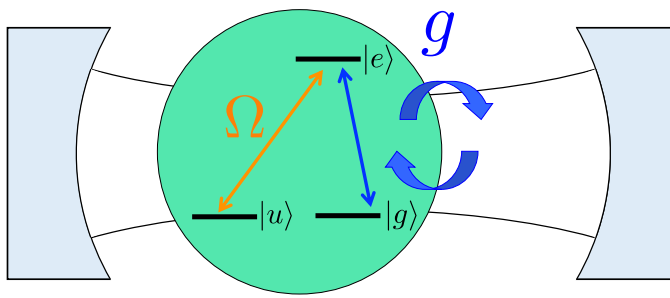

Fig. 8.5 Schematic of cavity QED system with a Λ-type three-level atom.

$$\hat{H}_{\mathrm{JC}\Lambda} = \hbar\omega_{\mathrm{A}}\hat{\sigma}_{eg}\hat{\sigma}_{ge} + \hbar\omega_{\mathrm{C}}\hat{a}_{\mathrm{c}}^{\dagger}\hat{a}_{\mathrm{c}} + \hbar g(\hat{\sigma}_{eg}\hat{a}_{\mathrm{c}} + \hat{\sigma}_{ge}\hat{a}_{\mathrm{c}}^{\dagger}) + \frac{\hbar\Omega}{2}(\hat{\sigma}_{eu}e^{-i\omega_L t} + \hat{\sigma}_{ue}e^{i\omega_L t}), \tag{8.34}$$

where $\hat{\sigma}_{ij} = |i\rangle\langle j|$, Ω represents the Rabi frequency of the amplitude of the external field, and ω_L represents the frequency of the external field.

Let us consider a case with no external field ($\Omega = 0$). If the atom is in $|g\rangle$, the optical response of the system is the same as that of the cavity QED system with a two-level atom; $r(\Delta_{\mathrm{p}} = 0) \approx 1$ for $\eta_{\mathrm{esc}} \approx 1$ and $C \gg 1$. However, if the arm is in $|u\rangle$, the system behaves as if there are no atoms, and $r(\Delta_{\mathrm{p}} = 0) \approx -1$ for $\eta_{\mathrm{esc}} \approx 1$ and $C \gg 1$. Therefore, the phase shift of π can be switched upon the reflection of a photon by changing the state of the atom. If the atom is in a superposition state of $|g\rangle$ and $|u\rangle$, the response of the system is the superposition of that of the atom in $|g\rangle$ and in $|u\rangle$. Thus, one can create entanglement between the atom and the photon by reflecting the photon.

Next, we consider the case of an external field ($\Omega \neq 0$). The Hamiltonian $\hat{H}_{\mathrm{JC}\Lambda}$ couples only the states within the group of $\{|u, n\rangle, |e, n\rangle, |g, n+1\rangle\}$, and therefore, its eigenstates are a superposition of these states, and their eigenenergies are [35]

$$E_{\mathrm{D}}^{(n)} = n\hbar\omega, \tag{8.35}$$

$$E_{\pm}^{(n)} = n\hbar\omega + \frac{\hbar}{2}\left[\Delta \pm \sqrt{\Delta^2 + 4g^2(n+1) + \Omega^2}\right]. \tag{8.36}$$

The eigenstates corresponding to $E_{\mathrm{D}}^{(n)} = n\hbar\omega$ are given by

$$|\mathrm{D}_n\rangle = \frac{2g\sqrt{n+1}|u, n\rangle + \Omega|g, n+1\rangle}{\sqrt{\Omega^2 + 4g^2(n+1)}}, \tag{8.37}$$

and are called "dark states" because they have no contribution from the atomic excited state $|e\rangle$. Eq. (8.37) indicates that the probability amplitudes of $|g\rangle$ and $|u\rangle$ in $|\mathrm{D}_n\rangle$ depend on the amplitude of control field Ω. Specifically, $|\mathrm{D}_n\rangle = |u, n\rangle$ for $\Omega = 0$, and $|\mathrm{D}_n\rangle \to |g, n+1\rangle$ for $\Omega \to \infty$. Therefore, the system state can be adiabatically converted from $|\mathrm{D}_n\rangle = |u, n\rangle$ to $|\mathrm{D}_n\rangle \to |g, n+1\rangle$ without excitation to $|e\rangle$ by slowly changing Ω from 0 to ∞, or the other way around by changing Ω from ∞ to 0 [35]. This adiabatic process in the cavity QED system is called the vacuum-stimulated Raman adiabatic passage (vSTIRAP) [36].

8.3.6 Waveguide quantum electrodynamics

Waveguides are also used to enhance atom-photon interactions. Transverse modes of light can be confined to a small mode area, and the dispersion can be considerably modified from that in free space. Therefore, efficient interaction between an atom and the propagating mode of the waveguide can be achieved by placing the atom inside the mode, as shown in Fig. 8.6.

Quantum photonics with photonic crystals

9

Takashi Asano[a], *Makoto Yamaguchi*[b], *Ryotaro Konoike*[c], *and Susumu Noda*[a,d]
[a]Department of Electronic Science and Engineering, Kyoto University, Kyoto-Daigaku-Katsura, Nishikyo-ku, Kyoto, Japan, [b]Department of Physics, Tokai University, Hiratsuka, Kanagawa, Japan, [c]Photonics Research Center, National Institute of Advanced Industrial Science and Technology (AIST), Tsukuba, Japan, [d]Photonics and Electronics Science and Engineering Center, Kyoto University, Kyoto-Daigaku-Katsura, Nishikyo-ku, Kyoto, Japan

9.1 Two-dimensional photonic crystals as a platform for quantum photonics

In this section, we discuss nanocavities based on point defects in slab-type two-dimensional (2D) photonic crystals (PCs), which are the most successful nanocavities from the viewpoint of high-Q factors with small cavity modal volumes (V_{cav}). The principle to confine light in a small space is explained, and the performances of the state-of-the-art PC nanocavities are shown.

9.1.1 Two-dimensional photonic crystal slabs

A 2D-PC slab, that is, a thin dielectric slab with a 2D periodic refractive index modulation, provides an important method to confine light in a 2D plane. This structure uses the 2D modulation of a refractive index to create a gap in the photonic mode spectrum (i.e., a photonic bandgap, or PBG) to confine light in the in-plane directions, and a large refractive index contrast between the slab and air-cladding to confine the light in the out-of-plane directions (Fig. 9.1A). Thin slab structures are generally utilized because thick structures that support multiple modes in the thickness dimension are difficult to be utilized for precise control of light. By introducing line defects (Fig. 9.1B) [1, 2] and point defects (Fig. 9.1C) [1, 3–9] into 2D-PC slabs, waveguides (WGs), and cavities can be formed, respectively. The former can provide precise dispersion control including slow light, flat dispersion, enhanced nonlinearity, etc. The latter can provide ultra-high Q cavities with small modal volumes, which are advantageous from the viewpoint of small footprint, large free-spectral range (FSR), strong light-matter interaction, etc.

Quantum Photonics. https://doi.org/10.1016/B978-0-323-98378-5.00010-6

9.2.2 Photonic quantum computation with waveguide-linked optical cavities and quantum dots

In Section 9.2.1, we have focused on the photon emission mechanism of a semiconductor QD inside a cavity. In particular, we should remember that the experimental studies are especially enabled by the development of techniques for deterministic positioning of the QDs [55, 56, 59] and the realization of the long cavity photon lifetime [6]. Such technical progresses can motivate us to realize photonic quantum bits (qubits) inside cavities and its deterministic control. In this context, here, in Section 9.2.2, we describe a possible scheme of QIP [44] by further using a concept of dynamic control of the cavity Q-factor [7, 43, 89]. In this approach, the photonic qubit is encoded in two distant optical cavities linked by a WG (Fig. 9.11) [7, 43], while the two-qubit operations are achieved by a single QD (treated as a V-type three-level system [90]) embedded in the intersection of two orthogonal WGs (Fig. 9.12). This scheme simultaneously permits a number of significant advances to be made:

- **(I)** It enables programmable operations because the optical length of the WGs can be controlled dynamically after determination of the device structure [89].
- **(II)** The single QD allows a deterministic CNOT operation to be achieved.
- **(III)** The system can be integrated and scaled up to many qubits with properly designed WGs [91], providing a scalable platform for quantum computation by itself.
- **(IV)** Finally, each unit described here is compatible with current photonic QIP schemes and could also play a key role in improving their performance.

Even though practical application of this scheme may require further developments of current technologies and designs, the proposal may call for and accelerate them for future implementation of on-chip photonic QIP.

9.2.2.1 One-qubit operations

First, we describe the ways in which encoding and one-qubit gate operations are performed by discussing the effective Hamiltonian of the system shown in Fig. 9.11, where the WG is evanescently coupled with the single-mode cavities (see also

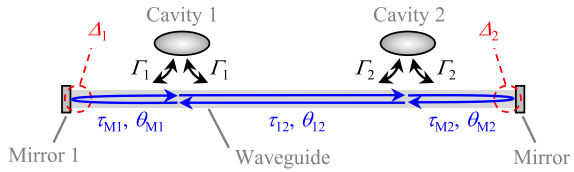

Fig. 9.11 Schematic picture of the proposed system for one-qubit operations. Δ_j is the phase change for the reflection at the jth mirror. τ_{M1}, τ_{M2}, and τ_{12} are the propagation times of light along the individual *arrowed lines*, while θ_{M1}, θ_{M2}, and θ_{12} are the corresponding phase changes caused by the propagation. Γ_ℓ is the photon emission rate from the ℓth cavity into one of the two opposite directions of the waveguide.
Reproduced from M. Yamaguchi, T. Asano, Y. Sato, S. Noda, Photonic quantum computation with waveguide-linked optical cavities and quantum dots, arXiv 2011, arXiv:1101.3508.

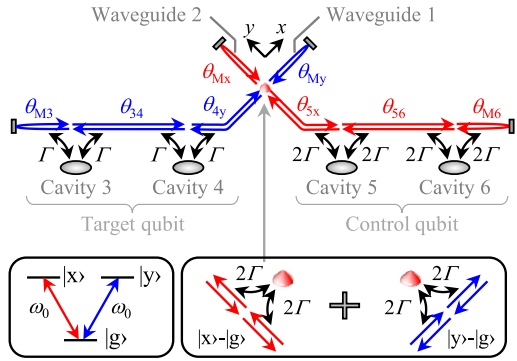

Fig. 9.12 Schematic picture of the system for two-qubit operation. The QD is treated as a V-type three-level system (*left inset*) where the $|x\rangle$-$|g\rangle$ transition is polarized in the x-direction and the $|y\rangle$-$|g\rangle$ transition is polarized in the y-direction. Therefore, each QD transition is allowed only for one of the orthogonal WGs (*right inset*). The eight θ's are the phase changes caused by the propagation of light along the *arrowed lines*.
Reproduced from M. Yamaguchi, T. Asano, Y. Sato, S. Noda, Photonic quantum computation with waveguide-linked optical cavities and quantum dots, arXiv 2011, arXiv:1101.3508.

Section 9.3.1 for experimental demonstrations). The Hamiltonian of this setup can be expressed as

$$\hat{H} = \sum_{\ell=1,2} \omega_{c,\ell} \hat{a}^{\dagger}_{c,\ell} \hat{a}_{c,\ell} + \sum_{\lambda\in\{FP\}} \omega_{\lambda} \hat{a}^{\dagger}_{\lambda} \hat{a}_{\lambda} + i \sum_{\ell=1,2} \sum_{\lambda\in\{FP\}} (g_{\ell,\lambda} \hat{a}_{c,\ell} \hat{a}^{\dagger}_{\lambda} + g^{*}_{\ell,\lambda} \hat{a}_{\lambda} \hat{a}^{\dagger}_{c,\ell}), \quad (9.23)$$

where $g_{\ell,\lambda} \equiv g^{L}_{\ell,\lambda} + g^{R}_{\ell,\lambda}$ is the coupling constant between the cavity modes and the Fabry-Pérot (FP) modes formed in the WG. Here, $\hat{a}_{c,\ell}$ denotes the annihilation operator for the single-optical mode in the ℓth cavity and $\hat{a}_{\lambda}$ is the annihilation operator for the λth FP mode. We note that this Hamiltonian can be derived as the quantization of classical coupled mode theory involving all of the input-output relations between incoming and outgoing waves [44]. The absolute values of $g^{i}_{\ell,\lambda}$ ($i = $ L, R and $\ell = 1, 2$) are expressed as $|g^{i}_{\ell,\lambda}| = \sqrt{\Gamma_{\ell}/\tau_{p}}$, where Γ_{ℓ} is the photon emission rate from the ℓth cavity into one of the two opposite directions of the WG and τ_{p} is the time taken for the light to propagate along the WG and back ($\tau_{p} = \tau_{M1} + \tau_{M2} + 2\tau_{12}$), as shown in Fig. 9.11. The phase differences of $g^{i}_{\ell,\lambda}$ are given by $\arg[g^{L}_{2,\lambda}] - \arg[g^{R}_{2,\lambda}] = \omega_{\lambda}\tau_{M2} + \Delta_{2}$ and $\arg[g^{L}_{1,\lambda}] - \arg[g^{R}_{2,\lambda}] = \arg[g^{R}_{2,\lambda}] - \arg[g^{R}_{1,\lambda}] = \omega_{\lambda}\tau_{12}$, where Δ_{j} is the change in phase that occurs when a photon is reflected at the jth mirror and τ_{M1}, τ_{M2}, and τ_{12} are the propagation times of light between the cavities. When both cavities have the same properties (i.e., resonant frequency $\omega_{c,1} = \omega_{c,2} \equiv \omega_{0}$ and emission rate $\Gamma_{1} = \Gamma_{2} = \Gamma_{c}$), elimination of the WG's degrees of freedom [44] gives the following effective Hamiltonian:

$$\hat{H}^{\text{eff}}_{1} = \sum_{\ell=1,2} \omega^{\text{eff}}_{c,\ell} \hat{a}^{\dagger}_{c,\ell} \hat{a}_{c,\ell} + g^{\text{eff}}_{12} (\hat{a}^{\dagger}_{c,1} \hat{a}_{c,2} + \text{h.c.}), \quad (9.24)$$

Optical lattice clocks and related platforms

10

Masao Takamoto[a,b] *and Hidetoshi Katori*[a,b,c]
[a]Quantum Metrology Laboratory, RIKEN, Wako, Saitama, Japan, [b]Space-Time Engineering Research Team, RIKEN, Wako, Saitama, Japan, [c]Department of Applied Physics, Graduate School of Engineering, The University of Tokyo, Bunkyo-Ku, Tokyo, Japan

10.1 Introduction

The unit of time, the second, was defined in 1967 by microwave transition in the hyperfine ground states of ^{133}Cs. Since the 1980s, laser cooling and trapping of atoms were developed, which enabled fine control of atomic motion and advanced the precision of atomic clocks. In atomic fountain clocks, laser-cooled atoms extend their interaction time with an electromagnetic field to about 1 s, achieving clock uncertainty of a few parts in 10^{16} [1], which sets the uncertainty of the second in the International System of Units (SI). High-precision atomic clocks are crucial in science and serve as a core technology in modern society, such as global navigation satellite systems (GNSS) and large-capacity, high-speed communication networks.

Atomic clocks have rapidly progressed in precision by employing optical frequencies. Since the invention of the laser in 1960, significant advances in coherent lasers, including narrow linewidth lasers [2,3] and optical frequency combs [4,5], have been made, constituting the technical foundation for optical clocks. For a given frequency measurement uncertainty $\Delta\nu$, which is primarily determined by the coherent interaction time $T(=1/\Delta\nu)$ between atoms and electromagnetic fields, the fractional uncertainty $\Delta\nu/\nu_0$ of a clock can be improved by increasing the atomic transition frequency ν_0. Moving to higher frequencies is advantageous as most systematic uncertainties do not scale with the frequency, except for the Doppler effect $\delta\nu_D = (v/c)\nu_0$ with v representing the velocity of an atom and c representing the speed of light. By removing the Doppler effect, an optical atomic clock should outperform a microwave cesium clock by four orders of magnitude.

So far, optical atomic clocks, such as single-ion clocks [6,7] and optical lattice clocks [8–10], have demonstrated uncertainties at 10^{-18} or below, which is more than two orders of magnitude better than those of cesium clocks. Discussions are underway to redefine the "second" by optical transitions [11]. Optical atomic clocks with unprecedented uncertainty and instability will serve as novel sensing devices for spacetime curved by gravity, i.e., "chronometric leveling," as well as a probe to explore fundamental physics, such as the constancy of the fundamental constants [12,13] and the search for dark matter [14]. This chapter provides an overview and

Quantum Photonics. https://doi.org/10.1016/B978-0-323-98378-5.00002-7

review of the basics of optical lattice clocks and their applications for precision measurements, including chronometric leveling and the testing of fundamental physics.

10.2 Optical atomic clocks

10.2.1 Indicators for atomic clocks: Uncertainty and instability

Atomic clocks should provide accurate reference frequency based on the atomic transition if the fundamental physical constants are constant and universal. The latter aspects make atomic clocks valuable tools for exploring the foundation of physics. The performance of the clocks is given by two indices, "uncertainty" and "instability." The transition frequency ν_0 of the reference atom can be affected by perturbations such as electromagnetic fields, atomic collisions, and atomic motion, resulting in a frequency shift $\delta\nu$. The "uncertainty" addresses the uncertainty in correcting for such systematic frequency shifts. The "instability" describes the statistical uncertainty for a given averaging time and is evaluated by the Allan deviation [15]. The instability is fundamentally limited by the quantum projection noise in measuring the atomic states and is practically limited by the frequency noise of the local oscillator (LO) probing the atoms. The schematic of an optical atomic clock is shown in Fig. 10.1, consisting of atoms and a laser stabilized to the atomic transition.

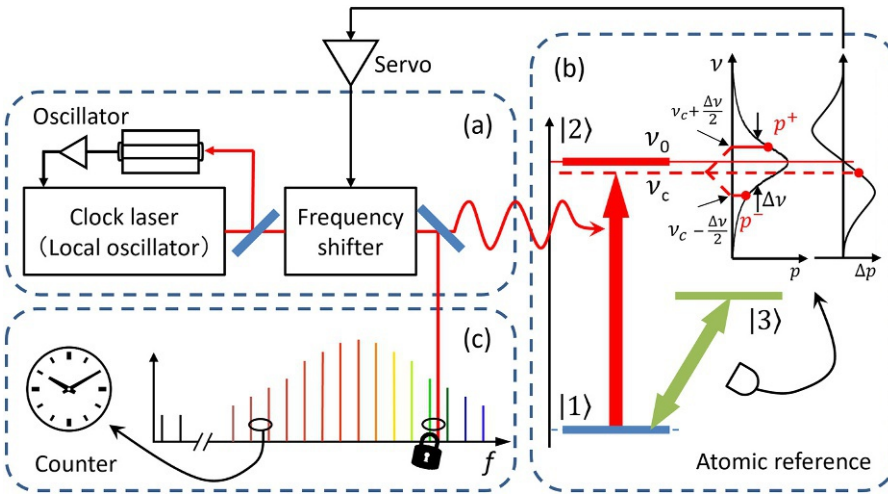

Fig. 10.1 A schematic of an optical atomic clock. A narrow-linewidth laser, stabilized to an optical reference cavity, excites the clock transition $|1\rangle \rightarrow |2\rangle$ of atoms. The excitation probability p is used to feedback-control the frequency shifter thus keeping the clock laser frequency ν_c resonant with the clock transition frequency ν_0. The excitation probability is determined by observing the fluorescence on the electric dipole-allowed transition $|1\rangle \rightarrow |3\rangle$. The optical frequency may be downconverted to an RF using a frequency comb.

Quantum key distribution and its applications

11

Masahiro Takeoka
Keio University, Yokohama, Kanagawa, Japan

11.1 Introduction

This chapter describes quantum cryptography. Quantum cryptography is one of the most successful applications of quantum optics and quantum information theory. The key technology of quantum cryptography is quantum key distribution (QKD), which can distribute secret keys that are unbreakable by any computational means or physical eavesdropping attacks. The chapter starts with a brief overview of the current cryptographies and their potential threats, then describes the security and basic operation principles of quantum cryptography. We will also see that quantum cryptography has already been deployed into the field testbed, and proof-of-concept demonstrations of its applications will soon be available in practical use.

11.2 Modern cryptography and quantum cryptography

Cryptography is an indispensable tool for securing current and future network society. Modern cryptosystems consist of common key cryptography and public key cryptography. The former, for example, Advanced Encryption Standard (AES), shares symmetric pairs of a secret key between the sender and the receiver, while the latter, e.g., Rivest-Shamir-Adelman (RSA), uses asymmetric keys: a secret key and public key. Both are based on mathematical algorithms and their security, more precisely, confidentiality, relies on the computational hardness of its cracking. The common key cryptos usually need seed keys that are typically supplied by the public key cryptos, and, in this system, security is bounded by the security of the public key cryptos that are used. The security of public key cryptos are guaranteed by mathematical problems that are hard to solve. Examples of such problems are factorization, used in RSA, and discrete logarithmic problems in elliptic curve cryptography. These problems require an extremely long time (on average) to solve, even with supercomputers, if the size of the problem is relatively large.

However, this type of security heavily relies on the computational power of a malicious third party (i.e., an "eavesdropper"). A quantum computer is recognized as a serious threat as known quantum algorithms can efficiently solve these problems, although large-scale, fault-tolerant quantum computers have yet to be developed.

For such a potential threat, there are two counterparts under development. The first approach is postquantum cryptography (PQC) [1]. PQC is still in a computational

Quantum Photonics. https://doi.org/10.1016/B978-0-323-98378-5.00001-5

Optical large-scale quantum computation

12

Kosuke Fukui and Shuntaro Takeda
Department of Applied Physics, The University of Tokyo, Tokyo, Japan

12.1 Introduction

Over the past decades, various quantum systems have been investigated as hardware platforms for quantum information processing (QIP). Optics is one of the most promising candidates for the platform since it has unique advantages that no other physical system offers. In optical systems, we can easily perform almost all quantum operations with only linear optics. Furthermore, these operations can be realized without preparing low-temperature or vacuum environments since light is inherently robust to environmental noise. These advantages have greatly progressed such optical QIP as quantum communication and quantum computing (QC). The approaches to optical QIP are generally classified into two types: the discrete-variable (DV) approach, which uses the particle nature of light, and the continuous-variable (CV) approach, which uses the wave nature of light. These two approaches have their own advantages and schemes for scalable optical QIP. This chapter will focus on optical quantum computation and address how it can be realized in scalable ways with DVs and CVs while comparing these two approaches.

In this chapter, we start by describing the fundamentals of optical quantum states for DV and CV QIP in Section 12.2. We then introduce optical quantum computation with DVs and CVs in Section 12.3. We define DV and CV quantum operations and briefly compare the differences between them. In Section 12.4, we explain the approaches for scalable optical quantum computation with DVs and CVs, describing how DV and CV quantum operations can be performed and used for large-scale quantum computation. We finally review DV and CV fault-tolerant quantum computation (FTQC) in Section 12.5, describing how errors during quantum computation can be corrected to achieve reliable results for quantum computation.

12.2 Optical quantum state

In the classical picture, light is electromagnetic waves, which can be explained by Maxwell's equations. In the quantum picture, light can be understood both as particles and waves, and these two features are used to encode the quantum information of qubits and qumodes, respectively. In this section, we will explain how the optical quantum states as qubits or qumodes are described and measured in optical QC.

Quantum Photonics. https://doi.org/10.1016/B978-0-323-98378-5.00012-X

12.3 Optical quantum computation

In this section, we will focus on how to manipulate optical quantum states by quantum gates and thereby perform arbitrary QC in DVs and CVs. Table 12.1 provides a summary of the comparison between DV and CV QC. For further study, reviews for QIP with DVs and CVs were provided in Refs. [2–4] and [5–9], respectively.

12.3.1 Quantum computation with discrete variables

QC has the potential to efficiently solve certain problems which are intractable with conventional computers. However, we need to prepare appropriate quantum gate sets to perform arbitrary QC and thereby extract the full power of QC. Quantum gates for qubits are classified into two groups: Clifford and non-Clifford gates. The Gottesman-Knill theorem for qubits [10] shows that a class of QC with qubits that employs only Clifford gates and projective measurements in the computational basis can be simulated efficiently by classical computers. Thus, non-Clifford gates play a vital role in providing a speedup over classical computers and achieving universality in QC. Here, the term "universality" means the ability to perform any unitary transformation with

Table 12.1 Comparison between DV and CV quantum information processing.

	Discrete variables (qubits)	**Continuous variables (qumodes)**
Computational basis	$\{\|0\rangle_{\mathrm{L}}, \|1\rangle_{\mathrm{L}}\}$	$\{\|s\rangle_q\}_{s\in\mathbb{R}}$
Conjugate basis	$\left\{\|\pm\rangle_{\mathrm{L}} = \frac{1}{\sqrt{2}}(\|0\rangle_{\mathrm{L}} \pm \|1\rangle_{\mathrm{L}})\right\}$	$\left\{\|t\rangle_p = \frac{1}{\sqrt{2\pi}}\int_{-\infty}^{\infty} ds \quad e^{ist}\|s\rangle_q\right\}_{t\in\mathbb{R}}$
Encoding	$\|\psi\rangle = \alpha\|0\rangle_{\mathrm{L}} + \beta\|1\rangle_{\mathrm{L}}$ $(\|\alpha\|^2 + \|\beta\|^2 = 1)$	$\|\psi\rangle = \int_{-\infty}^{\infty} ds \quad \psi(s)\|s\rangle_q$ $(\int_{-\infty}^{\infty} ds\|\psi(s)\|^2 = 1)$
Detector	Photon detector	Homodyne detector
	Bit-flip gate: $\hat{X}$	Displacement in $\hat{q}$: $\hat{X}(v) = e^{-iv\hat{p}}$ $(v \in \mathbb{R})$
	$\hat{X}\|0\rangle_{\mathrm{L}} = \|1\rangle_{\mathrm{L}}, \hat{X}\|1\rangle_{\mathrm{L}} = \|0\rangle_{\mathrm{L}}$	$\hat{X}(v)\|s\rangle_q = \|s+v\rangle_q$
	Phase-flip gate: $\hat{Z}$	Displacement in $\hat{p}$: $\hat{Z}(u) = e^{iu\hat{q}}$ $(u \in \mathbb{R})$
	$\hat{Z}\|0\rangle_{\mathrm{L}} = \|0\rangle_{\mathrm{L}}, \hat{Z}\|1\rangle_{\mathrm{L}} = -\|1\rangle_{\mathrm{L}}$	$\hat{Z}(u)\|t\rangle_p = \|t+u\rangle_p$
Quantum gate	Hadamard gate: $\hat{H}$	Fourier gate: $\hat{R}\left(\frac{\pi}{2}\right) = e^{i\frac{\pi}{4}(\hat{q}^2+\hat{p}^2)}$
	$\hat{H}\|0\rangle_{\mathrm{L}} = \|+\rangle_{\mathrm{L}}, \hat{H}\|1\rangle_{\mathrm{L}} = \|-\rangle_{\mathrm{L}}$	$\hat{R}\left(\frac{\pi}{2}\right)\|s\rangle_q = \|s\rangle_p, \hat{R}\left(\frac{\pi}{2}\right)\|t\rangle_p = \|-t\rangle_q$
	Controlled-NOT (CX) gate: $\widehat{CX}$	CX gate: $\widehat{CX} = e^{-i\hat{q}_1\hat{p}_2}$
	$\widehat{CX}\|0\rangle_{\mathrm{L}}\|0(1)\rangle_{\mathrm{L}} = \|0\rangle_{\mathrm{L}}\|0(1)\rangle_{\mathrm{L}}$	$\widehat{CX}\|s_1\rangle_{q_1}\|s_2\rangle_{q_2} = \|s_1\rangle_{q_1}\|s_2+s_1\rangle_{q_2}$
	$\widehat{CX}\|1\rangle_{\mathrm{L}}\|0(1)\rangle_{\mathrm{L}} = \|1\rangle_{\mathrm{L}}\|1(0)\rangle_{\mathrm{L}}$	$\widehat{CX}\|t_1\rangle_{p_1}\|t_2\rangle_{p_2} = \|t_1-t_2\rangle_{p_1}\|t_2\rangle_{p_2}$
Carrier	Degrees of freedom of a photon	Quadratures of a light field